processes

Article

Effects of Albedo and Thermal Inertia on Pavement Surface Temperatures with Convective Boundary Conditions—A CFD Study

Tathagata Acharya [1,*], Brooke Riehl [1,2] and Alan Fuchs [3]

[1] Department of Physics and Engineering, California State University, Bakersfield, CA 93311, USA; briehl@csub.edu
[2] McIntosh & Associates Engineering, Inc., Bakersfield, CA 93309, USA
[3] Dean's Office, California State Polytechnic University, Pomona, CA 91768, USA; afuchs@cpp.edu
* Correspondence: tacharya@csub.edu

Abstract: The urban heat island (UHI) effect increases the ambient temperatures in cities and alters the energy budget of building materials. Urban surfaces such as pavements and roofs absorb solar heat and re-emit it back into the atmosphere, contributing towards the UHI effect. Over the past few decades, researchers have identified albedo and thermal inertia as two of the most significant thermal properties that influence pavement surface temperatures under a given solar load. However, published data for comparisons of albedo and thermal inertia are currently inadequate. This work focuses on asphalt and concrete as two important materials used in the construction of pavements. Computational fluid dynamics (CFD) analyses are performed on asphalt and concrete pavements with the same dimensions and under the same ambient conditions. Under given conditions, the pavement top surface temperature is evaluated with varying albedo and thermal inertia values. The results show that the asphalt surface temperatures are consistently higher than the concrete surface temperatures. Surface temperatures under solar load reduce with increasing albedo and thermal inertia values for both asphalt and concrete pavements. The CFD results show that increasing the albedo is more effective in reducing pavement surface temperatures than increasing the thermal inertia.

Keywords: albedo; thermal inertia; CFD; pavement materials

Citation: Acharya, T.; Riehl, B.; Fuchs, A. Effects of Albedo and Thermal Inertia on Pavement Surface Temperatures with Convective Boundary Conditions—A CFD Study. *Processes* **2021**, *9*, 2078. https://doi.org/10.3390/pr9112078

Academic Editor: Ireneusz Zbicinski

Received: 5 November 2021
Accepted: 16 November 2021
Published: 19 November 2021

1. Introduction

The urban heat island (UHI) effect is a phenomenon whereby higher temperatures are experienced in urban areas compared to the countryside. The UHI effect has been a subject of interest since the 19th century, when Howard showed that the air temperatures in a city were higher than the surrounding countryside [1]. During the last decade, the ever-increasing threat of global warming has resulted in UHIs being a research area of tremendous importance [2–4]. Cities occupy approximately 2% of earth's surface; however, city dwellers consume approximately 75% of the earth's total energy resources [5]. The urban population of the world is rapidly increasing as more people are leaving rural areas to settle down in the cities. The UHI effect is illustrated by graphically mapping temperatures across cities and comparing those against temperatures in the countryside immediately surrounding them. The larger temperature spikes at the center of the graph represent the 'heat island', with higher city temperatures [6–8].

Figure 1 shows how a UHI occurs in a city. Solar heat during the day is absorbed by various urban surfaces such as the roofs of buildings and pavements. Heat is transferred back into the atmosphere from these surfaces. The air nearer to the surfaces on earth are warmer due to heat transfer. Heat is also released from factories, automobiles, and other anthropogenic sources.

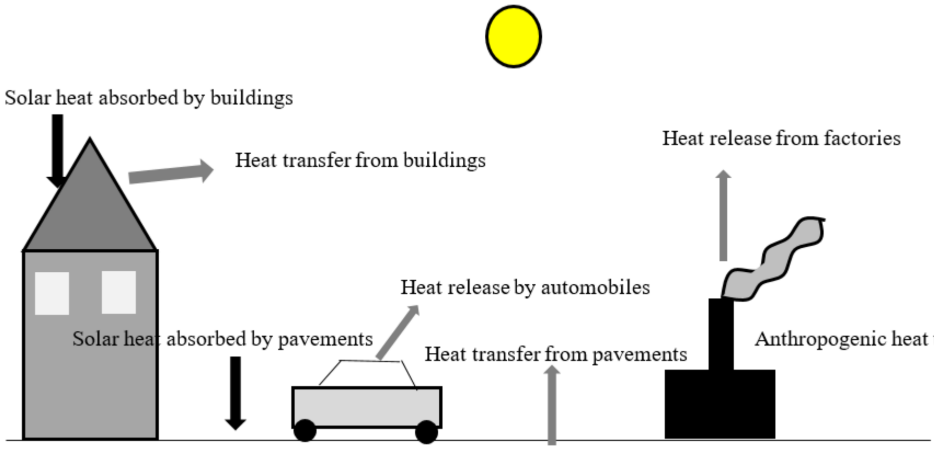

Figure 1. The urban heat island (UHI) effect in cities.

The UHI effect has detrimental consequences for the health and well-being of people living in cities worldwide [9–11]. According to various reports, the Center for Disease Control and Prevention in the United States attributed 7421 deaths between 1979 and 1998 in United States to UHIs [12,13]. Researchers have shown that city temperatures locally rise because of the way they are structured. The increased use of synthetic materials with low reflectivity and anthropogenic heat production are prime causes of UHIs [14–16]. The heat island effect also results from dwindling vegetation, reductions in evapotranspiration in cities, and the prevalence of darker objects in urban architecture [17]. Previous researchers have estimated that over 60% of urban surfaces are covered by synthetic heat-absorbent materials, of which approximately 40% are pavements [18].

Pavements contribute significantly to the UHI effect. Mesoscale images from satellites have revealed that urban pavements are significant sources of thermal activity and heat radiation [15]. Urban surfaces such as pavements absorb solar energy and radiate it back to the atmosphere, contributing to UHIs. Therefore, one way to assess UHIs is by studying the materials used in urban infrastructure such as pavements, building materials, and roofs. Various researchers have focused on the choices of materials used to build pavements and performed experiments to study heat retention and emissions associated with pavement materials [19–21]. In a recent article, researchers studied pavement damages due to overweight vehicles using a novel framework [22]. Asphalt and concrete are the most common materials used for pavement construction.

Knowledge of radiative properties such as emissivity and albedo are very essential in studying heat transfer from pavements. Emissivity is defined as the relative measure of the total energy emitted across all wavelengths by an object in comparison to a blackbody at the same temperature. This is given by Equation (1):

$$\varepsilon = \frac{q}{q_b}, \tag{1}$$

where ε is the emissivity of the surface, q is the energy emitted per unit area by the surface, and q_b is the energy emitted per unit area by a blackbody. Researchers have shown that emissivity increases with increases in roughness [23–26].

Albedo is defined as the fraction of incident solar light that is reflected from a material surface, which is given by Equation (2):

$$Albedo = \frac{reflected\ solar\ radiation}{incident\ solar\ radiation} \tag{2}$$

Most surfaces that are darker in color have lesser albedo than surfaces that are brighter in color. The albedo of a perfect blackbody is zero [10,27–30]. However, there may also be some surfaces that are dark colored and reflect large portions of infrared solar radiation. These surfaces may also have high albedos [31].

Many previous articles reported experimental results showing heat loss from different materials under specific ambient conditions. These articles measured surface temperatures on materials such as asphalt, cement, bare soil, and grass [20,32–36]. A couple of recent articles discussed pavement solar collector (PSC) technology, where pavement heat is utilized for recharging shallow geothermal boreholes during summer [37,38]. Many of the articles reported comparisons between asphalt and concrete pavements in terms of their contributions to UHIs. Although several reports suggested that asphalt contributes to the heat island effect more than concrete, at least one article suggested otherwise [39]. Many articles have reported on empirical models studying pavement surface temperatures. However, many of these models exclude critical parameters such as albedo and thermal inertia.

Computational fluid dynamics (CFD) is widely used to study urban physics. Specific applications include pollutant dispersion [40–43], natural ventilation [11,44,45], and pedestrian-level wind conditions [46–49]. However, fewer articles exist that focus on pedestrian level thermal comfort, such as the evaluation of pavement temperatures and heat transfer [50–52]. To the best of our knowledge, no article has reported the use of CFD for the analysis of critical parameters such as albedo and thermal inertia. Thermal inertia is defined as the property of a material that expresses the degree of slowness with which the temperature of the material reaches that of the environment [53]. It is given by Equation (3):

$$P = \sqrt{k\rho C_p}, \quad (3)$$

where P is the thermal inertia, k is the thermal conductivity, and C_p is the specific heat of the material. In the present work, the surface temperatures of two common pavement materials, asphalt and concrete, are evaluated under specific ambient conditions and a solar load using CFD and a radiation model. The model used for analysis has been validated against experimental results by previous researchers [19]. In this article, the effects of albedo on the surface temperature of both asphalt and concrete pavements under given ambient conditions are studied. Additional simulations are performed to study the variation in pavement top surface temperature with changing thermal inertia.

2. Materials and Methods

The following section details the numerical model that was developed and validated against experiments by previous researchers. The validated model was used to perform the sensitivity analysis of the pavement materials to albedo and thermal inertia. The results were used to compare the effects of varying albedo versus varying thermal inertia on the pavement materials and can be used by future researchers to evaluate effective pavement cooling strategies.

Three-dimensional CFD simulations were performed on pavement blocks made of two different materials—asphalt and concrete. The simulation geometry was based on Asaeda et al.'s 1991 experiments on asphalt and concrete pavement blocks. Similar to the experiments, the pavement structures used in the model were rectangular, having the same dimensions. The structures were 3 m in length, 3 m in width, and 0.1 m in thickness. The experiments were performed in an open space. The wind velocity and ambient temperature were measured 1.5 m above the ground [19]. Inside pavement samples, 1-mm-diameter copper tubes were installed along the central axis at depths of 0.025 m, 0.05 m, and 0.1 m. Temperatures were measured by inserting thermocouples into the tubes [19]. Figure 2 shows the simulation geometry with the pavement block located in the center. The arrows show the direction of wind flow. In order for the pavement to be located in an open space, a 15 m long and 15 m wide simulation domain was created with the pavement located at the center. The domain was 1.5 m high based on the wind velocity measurement location given by Asaeda et al.

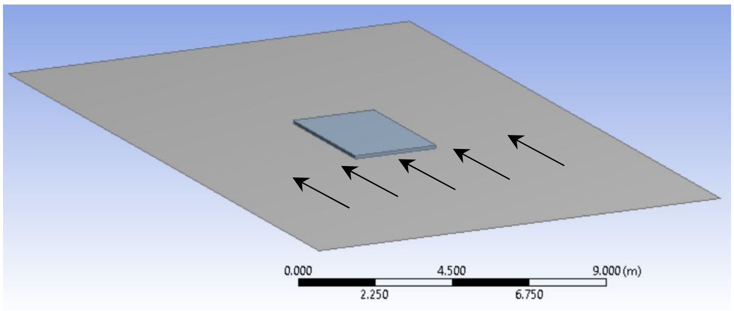

Figure 2. Simulation geometry.

ANSYS Fluent 18.2 was used for CFD simulations [54]. The simulation results were compared against Asaeda et al.'s experimental measurements of pavement top surface temperatures at a given date and time with the wind flowing at a certain velocity. In order to reduce the computational costs, the unsteadiness associated with the heat storage of pavement materials was ignored in the simulations. The steady-state temperature on the pavement top surface was calculated at a given wind speed at a given date and time. The model includes mass, momentum, and energy conservation equations. The flow is incompressible because the local changes in density are small. The mass conservation equation is given by Equation (4):

$$\frac{\partial \rho}{\partial t} + \nabla \cdot (\rho u) = 0, \tag{4}$$

where ρ is the density of the fluid and u is the flow velocity. Therefore, the mass conservation equation can be rewritten as:

$$\nabla \cdot u = 0, \tag{5}$$

Navier–Stokes equations are used for momentum conservation and are given by Equation (6):

$$\frac{\partial u}{\partial t} + u \cdot \nabla u = \frac{-1}{\rho}\nabla P + \frac{\mu}{\rho}\nabla^2 u + \frac{1}{\rho}F, \tag{6}$$

where ∇P is the pressure gradient, μ is the dynamic viscosity of the fluid, and F represents the body forces. The Boussinesq model is used for the density–temperature correlation, meaning Equation (6) can be re-written as:

$$\frac{\partial u}{\partial t} + u \cdot \nabla u = \frac{-1}{\rho}\nabla P + \frac{\mu}{\rho}\nabla^2 u - g\alpha\Delta T, \tag{7}$$

where g is the acceleration due to gravity, α is the thermal expansion coefficient, and ΔT is the change in temperature. Since the heat capacity of the material is assumed constant, the energy equation is given by Equation (8):

$$\frac{\partial T}{\partial t} + u \cdot \nabla T = \beta\nabla^2 T + \frac{J}{\rho C_p}, \tag{8}$$

where β is thermal diffusivity, J is the rate of internal heat production per unit volume, and C_p is the specific heat at constant pressure.

The 'discrete ordinates' radiation model was used with the 'solar ray tracing' algorithm. The solar ray tracing algorithm has been reported in several articles [52,55–59]. An important input to the model is the solar load acting on the pavement surface. The solar load depends on the solar angle of incidence, as well as pavement surface properties such as absorption and reflection. The solar ray tracing algorithm in ANSYS Fluent was used because it tracks the global position of the sun at a given time in the year. The solar calculator was used to indicate the sun's direction relative to the location of the pavement and to calculate solar irradiation at a specific date, time, and location. The study used the fair weather conditions method, as defined by ASHRAE, to calculate the direct and diffuse solar irradiation on the Earth's surface. The normal direct irradiation for fair weather conditions is given by Equation (9):

$$Edn = \frac{A}{B/e^{\sin\beta}}, \tag{9}$$

where Edn is the direct normal irradiation at the earth's surface, A is the apparent solar irradiation when the mass of air is 0, and B is the atmospheric extinction coefficient. Here, β is the solar altitude above the horizontal [55,56,60]. Infrared radiation is modeled using Equation (10):

$$Q_{IR} = \propto A_i \sigma {T_b}^4, \tag{10}$$

where Q_{IR} is the infrared radiation from the atmosphere, since the atmosphere can be treated as a blackbody for simplicity; T_b is the blackbody temperature; α is the absorptivity of the pavement material [55].

The hexahedral mesh is used and mesh independence is obtained with 2,797,202 elements in the simulation geometry. Figure 3 shows the mesh independency test results based on the calculated pressure at the domain inlet. The result does not change through three decimal places when the number of mesh elements exceeds 2.5 million.

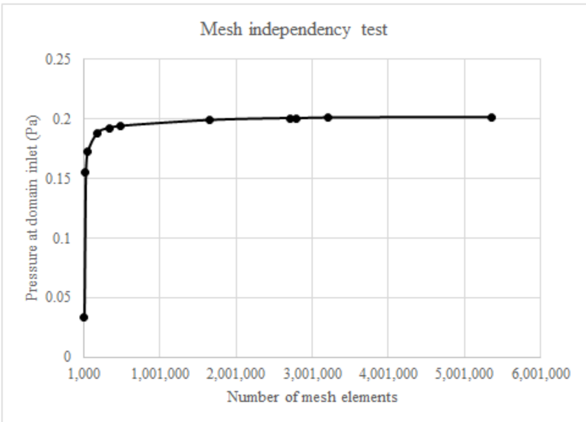

Figure 3. Mesh independency est.

In order to model the near wall behavior, scalable wall functions were used. Wall functions are a set of semi-empirical formulas and functions that connect the solution variables to the nearby wall cells with the corresponding quantities on the wall [61]. Scalable wall functions avoid the deterioration of standard wall functions with finer mesh sizes. The non-dimensional wall distance (y*) used in the mesh was 11.03. Figure 4 shows the mesh around the pavement geometry.

Based on Asaeda et al.'s experiment, in the model wind flows in one direction only. The free stream temperature is 305 K (32 °C) and the wind velocity is approximately 0.6 m/s [19]. In the model, a uniform velocity boundary condition is used at the inlet. The realizable k-ε turbulence model is used. At the inlet, the turbulence intensity and eddy viscosity ratio are imposed. While the eddy viscosity ratio is set as 10, the turbulence intensity is 5%. The eddy viscosity ratio is convenient to use in low-turbulence cases where it is difficult to estimate the turbulent length scale.

At the pavement surface, the stationary wall boundary condition is used with combined radiation and convection boundary conditions. Surface roughness is not specified. Table 1 shows the properties of the materials used at the surfaces [19].

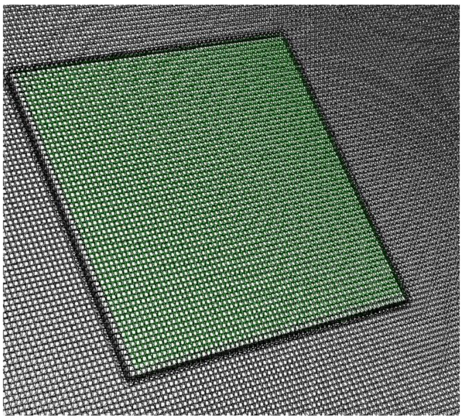

Figure 4. Mesh around the pavement geometry.

Table 1. Material properties.

Property	Asphalt	Concrete	Ground
Density, kg/m^3	2243	1800	1200
Specific Heat, J/kg K	633	1150	958
Thermal Conductivity, W/m K	0.74	1.69	0.04
Emissivity	0.94	0.94	0.94
Reflectivity	0.1	0.45	0.15

From the wind velocity, the Reynolds number is calculated using Equation (11):

$$Re = {}^{\rho v D_h}/_{\mu}, \quad (11)$$

where Re is the Reynolds number, ρ is the density of air in kg/m^3, v is the wind velocity in m/s, D_h is the characteristic length scale or width of the pavement block in m, and μ is the dynamic viscosity of air in Pa-s. The Nusselt number is calculated from the Reynolds number. Equation (12) is used when the flow is laminar:

$$Nu_L = 0.664 Re^{0.5} Pr^{1/3}, \quad (12)$$

where Nu_L is the average Nusselt number when the flow is laminar, Re is the Reynolds number, and Pr is the Prandtl number.

Equation (13) is used when the flow is turbulent:

$$Nu_T = 0.037 Re^{0.8} Pr^{1/3}, \quad (13)$$

where Nu_T is the average Nusselt number when the flow is turbulent. The convection coefficient is evaluated using the Nusselt number as shown by Equation (14):

$$Nu = {}^{hL}/_{k}, \quad (14)$$

where Nu is Nusselt number for both laminar and turbulent flows, h is the convection coefficient, L is the characteristic length scale, and k is the thermal conductivity of the material.

For pressure–velocity coupling, the SIMPLE algorithm scheme is used. Table 2 shows the settings used for spatial discretization:

Table 2. Spatial discretization.

Parameters	Methods
Gradient	Least Squares Cell-Based
Pressure	Second Order
Momentum	Second Order Upwind
Turbulent Kinetic Energy	First Order Upwind
Turbulent Dissipation Rate	First Order Upwind
Energy	Second Order Upwind
Discrete Ordinates	First Order Upwind

As the criteria for convergence, the residuals for all equations are set as 10^{-6}.

3. Results and Discussions

3.1. Model Validation

The CFD model was developed based on Asaeda et al.'s experiments on asphalt and concrete pavements performed in Tokyo, Japan (global position: longitude = 139.77°, latitude = 35.67°, time zone = 9) on 26 August 1991 [19]. The experiments were performed on asphalt and concrete pavements measuring each 3 m × 3 m × 0.1 m. Asaeda et al. reported an approximate ambient temperature of 305 K and wind speed of 0.6 m/s. The average wind speed was measured within an altitude of 1.5 m above the ground. The emissivity of both asphalt and concrete pavements was reported as 0.94. They reported a reflectivity of 0.1 for the asphalt pavement and a reflectivity of 0.45 for the concrete pavement. Using CFD, the pavement top surface temperature and the temperatures at depths of 2.5 cm, 5 cm, 7.5 cm, and 10 cm from the pavement top surface were calculated for a known ground temperature for both asphalt and concrete under the above-mentioned conditions at a given time of day (14:00). Figure 5 shows a comparison between the CFD results and the experimental measurements for the asphalt and concrete pavements.

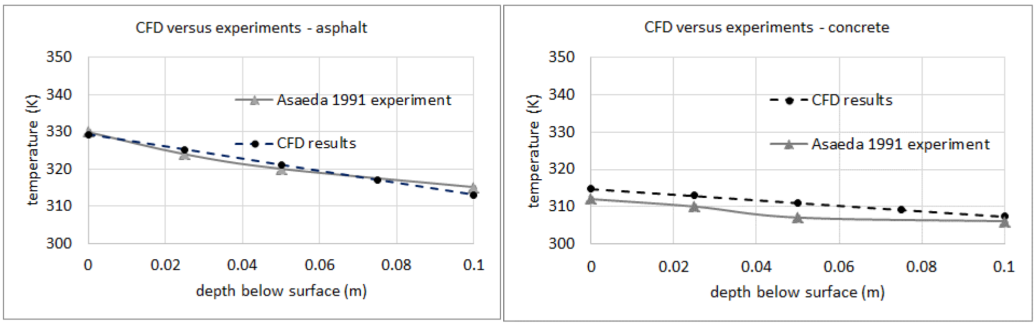

Figure 5. Validation of CFD results against experimental results shown by previous researchers.

The CFD results were in agreement with the experiments, with the top surface temperature difference being in the range of 1–2 K between the CFD results and experiments for the asphalt pavement. For the concrete pavement, the top surface temperature difference between the CFD results and experiments was approximately 3 K. Both CFD and experimental results showed that the top surface temperature of the concrete pavement was at least 15 K cooler than the corresponding asphalt pavement under identical ambient conditions. The slight difference in the top surface temperatures between the CFD and experimental results may be attributed to moisture in air, which the CFD model does not include. Asaeda et al. reported a humidity ratio of approximately 0.015.

The CFD model was used to assess asphalt and concrete pavement surface temperatures with varying albedo and thermal inertia values.

3.2. Surface Temperatures with Varying Albedo Values

The validated model was used to simulate the pavement surface temperatures with varying albedo values. The CFD model was used to evaluate surface temperatures of both asphalt and concrete pavements under given ambient conditions. An identical date and time of year (26 August, 14:00) were chosen for CFD analysis, when the ambient conditions were expected to be hot.

The pavement top surface temperature was evaluated at a wind speed of 1 m/s. The ambient temperature was 305 K. The direct normal solar irradiation at the location was 891.449 W/m^2. Asphalt pavements are typically darker in color, have high absorptivity, and low albedo values. The albedo value of the asphalt pavement can be increased by painting it with lighter colors. Previous researchers have reported albedo values of 0.1, 0.27, 0.4, and 0.55 for black, red or green, yellow, and off-white pavements, respectively [10]. Simulations were performed with albedo values varying from 0.1 to 0.9 and the same material properties for the asphalt. Figure 6 shows the temperature profile around the asphalt pavement with an albedo value of 0.1. The top surface temperature of the pavement was approximately 340 K.

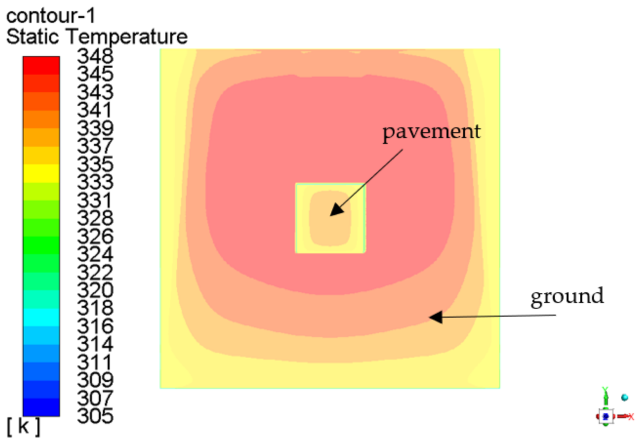

Figure 6. Temperature profile with asphalt albedo value of 0.1.

Figure 7 shows the temperature profile around the asphalt pavement with an albedo value of 0.9. The top surface temperature of the pavement was 322 K.

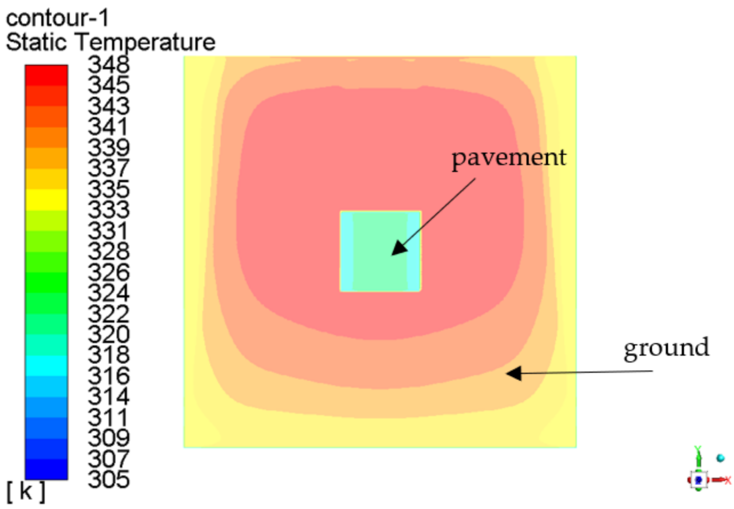

Figure 7. Temperature profile with asphalt albedo value of 0.9.

Figure 8 shows asphalt pavement surface temperatures with increasing albedo values. The result show that the surface temperature is approximately reduced by 2.3 K as the albedo increases by a value of 0.1. The pavement surface temperature linearly decreases with increasing albedo.

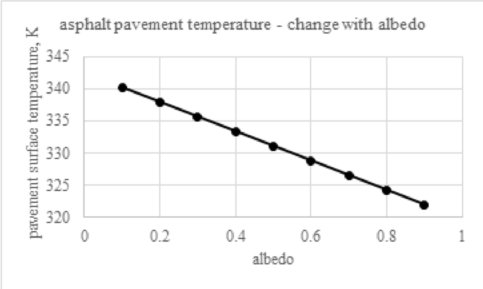

Figure 8. Asphalt pavement top surface temperatures with changing albedo values.

Simulations were performed with the concrete pavement under the same conditions. Typical albedo values for new concrete pavements range from 0.3 to 0.75 [62,63]. The other material properties of the concrete were unchanged. Figure 9 shows the concrete pavement surface temperatures with changing albedo values. The results show a temperature drop of approximately 1.05 K as the albedo is increased by 0.1 in concrete pavements. Therefore, the reduction in temperature with the increase in albedo is larger in asphalt than in concrete.

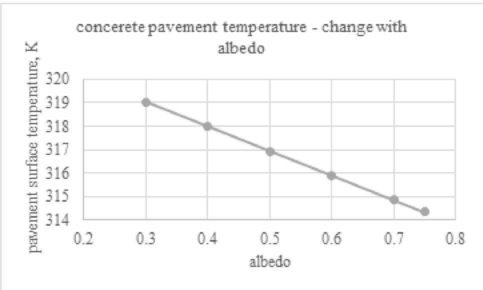

Figure 9. Concrete pavement top surface temperatures with changing albedo values.

3.3. Surface Temperatures with Varying Thermal Inertia Values

The thermal inertia of urban construction materials is related to the thermal properties of the urban fabric, such as the thermal conductivity, specific heat, and density. This is associated with a material's ability to store or lose heat [64,65]. The thermal inertia of the pavement may be varied by introducing filler materials [11,66].

In order to study the effects of thermal inertia, the thermal conductivity of asphalt was varied from 0.8 W/mK to 1.5 W/mK in intervals of 0.1. The density and specific heat of the material were unchanged. The albedo of the asphalt surface was kept constant at 0.1. The ambient conditions were the same as the albedo simulations and the wind speed was also 1 m/s.

Figure 10 shows the variations in top surface temperature of the asphalt pavement with changes in thermal inertia. The top surface temperature of the asphalt pavement drops by approximately 14 K as the thermal inertia is increased from 1065 $J/m^2Ks^{1/2}$ to 1459 $J/m^2Ks^{1/2}$.

For the concrete pavement, the albedo was kept constant at 0.3, with the same ambient conditions, wind speed, and wind direction. Figure 11 shows the variations in concrete top surface temperature with thermal inertia as the thermal conductivity of concrete is increased from 1.7 W/mK to 2.4 W/mK in intervals of 0.1 W/mK. The concrete pavement surface temperature drops by approximately 4 K only as the thermal inertia increases from 1875 $J/m^2Ks^{1/2}$ to 2229 $J/m^2Ks^{1/2}$.

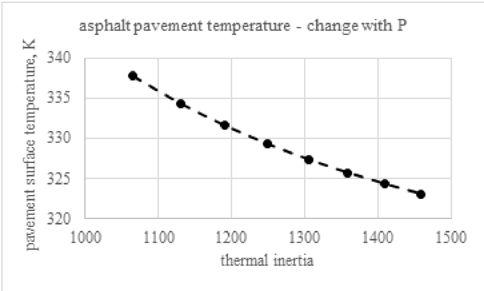

Figure 10. Asphalt pavement surface temperatures with changing thermal inertia values.

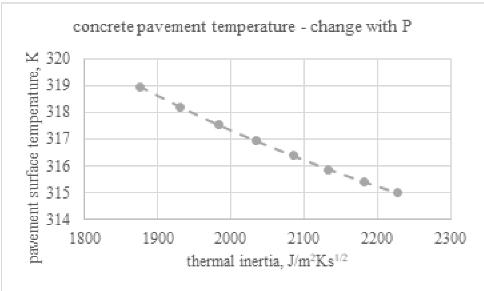

Figure 11. Asphalt pavement surface temperatures with changing thermal inertia values.

4. Conclusions

In this article, the comparative influence of albedo and thermal inertia values on pavement surface temperatures under a given solar load was investigated, which is a relatively unexplored area. The results from the study could be useful in developing pavement cooling strategies. The top surface temperatures of asphalt and concrete pavements were studied as functions of surface albedo and thermal inertia values. A solar radiation model was used in conjunction with CFD to calculate the solar heat flux based on a global position and the time of year. This model was validated against experimental results by previous researchers at a different location.

The results primarily showed that changing the surface albedo values of pavement materials is more effective in reducing pavement top surface temperatures than increasing the thermal inertia. Therefore, as opposed to the general practice, increasing the thermal inertia alone may not be sufficient to reduce pavement surface temperatures under given ambient conditions.

Secondly, this article presented a sensitivity analysis of pavement material top surface temperatures to albedo values, which to the best of our knowledge had not been reported before. The analysis showed that the top surface temperatures of the asphalt pavement decreased by 2–3 K for every 0.1 unit increase in albedo, while the corresponding concrete top surface temperature decreased by 1–2 K for every 0.1 unit increase in albedo. In addition, the asphalt pavement surface temperatures were consistently higher than corresponding concrete pavement surface temperatures. The higher temperatures in asphalt were due to the lower thermal conductivity and lower albedo values as compared to concrete.

Author Contributions: Conceptualization, T.A. and A.F.; methodology, T.A. and B.R.; software, T.A. and B.R; validation, T.A.; formal analysis, T.A.; investigation, T.A. and B.R.; resources, T.A. and A.F.; data curation, T.A. and B.R.; writing—original draft preparation, T.A.; writing—review and editing, T.A. and A.F.; visualization, T.A. and A.F.; supervision, A.F.; project administration, A.F.; funding acquisition, A.F. All authors have read and agreed to the published version of the manuscript.

Funding: This research was funded by Mineta Transportation Institute, grant number ZSB12017-SJAUX.

Institutional Review Board Statement: Not applicable.

Informed Consent Statement: Not applicable.

Data Availability Statement: Raw data were generated at California State University, Bakersfield. Derived data supporting the findings of this study are available from the corresponding author (T.A.) on request.

Acknowledgments: The authors acknowledge CSUB engineering students Spencer Schaffer and Martin Mendoza for their help with administrative activities.

Conflicts of Interest: The authors declare no conflict of interest.

References

1. Howard, L. *The Climate of London: Deduced from Meteorological Observations Made in the Metropolis and at Various Places Around It*; Harvey and Darton: London, UK, 1833; Volume 1.
2. Mavrogianni, A.; Davies, M.; Batty, M.; Belcher, S.E.; Bohnenstengel, S.I.; Carruthers, D.; Chalabi, Z.; Croxford, B.; Demanuele, C.; Evans, S.; et al. The comfort, energy and health implications of London's urban heat island. *Build. Serv. Eng. Res. Technol.* **2011**, *32*, 35–52. [CrossRef]
3. Ren, Z.; Wang, X.; Chen, D.; Wang, C.; Thatcher, M. Constructing weather data for building simulation considering urban heat island. *Build. Serv. Eng. Res. Technol.* **2014**, *35*, 69–82. [CrossRef]
4. Levermore, G.J.; Parkinson, J.B.; Laycock, P.J.; Lindley, S. The urban heat island in Manchester 1996–2011. *Build. Serv. Eng. Res. Technol.* **2015**, *36*, 343–356. [CrossRef]
5. Madlener, R.; Sunak, Y. Impacts of urbanization on urban structures and energy demand: What can we learn for urban energy planning and urbanization management? *Sustain. Cities Soc.* **2011**, *1*, 45–53. [CrossRef]
6. Bornstein, R.D. Observations of the urban heat island effect in New York City. *J. Appl. Meteorol.* **1968**, *7*, 575–582. [CrossRef]
7. Oke, T.R. The energetic basis of the urban heat island. *Q. J. R. Meteorol. Soc.* **1982**, *108*, 1–24. [CrossRef]
8. Grimmond, S. Urbanization and global environmental change: Local effects of urban warming. *Geogr. J.* **2007**, *173*, 83–88. [CrossRef]
9. Ichinose, T.; Futoshi, M.; Kumi, K. Counteracting urban heat islands in Japan. In *Urban Energy Transition*; Elsevier: Amsterdam, The Netherlands, 2008; pp. 365–380.
10. Synnefa, A.; Karlessi, T.; Gaitani, N.; Santamouris, M.; Assimakopoulos, D.N.; Papakatsikas, C. Experimental testing of cool colored thin layer asphalt and estimation of its potential to improve the urban microclimate. *Build. Environ.* **2011**, *46*, 38–44. [CrossRef]
11. Chen, J.; Wang, H.; Li, M.; Li, L. Evaluation of pavement responses and performance with thermal modified asphalt mixture. *Mater. Des.* **2016**, *111*, 88–97. [CrossRef]
12. Wolfe, M.I.; Kaiser, R.; Naughton, M.P.; Mirabelli, M.C.; Yoon, S.S.; Hanzlick, R.; Henderson, A.K. Heat-related mortality in selected United States cities, summer 1999. *Am. J. Forensic Med. Pathol.* **2001**, *22*, 352–357. [CrossRef]
13. Santamouris, M. Using cool pavements as a mitigation strategy to fight urban heat island—A review of the actual developments. *Renew. Sust. Energy Rev.* **2013**, *26*, 224–240. [CrossRef]
14. Satterthwaite, D. Cities' contribution to global warming: Notes on the allocation of greenhouse gas emissions. *Environ. Urban.* **2008**, *20*, 539–549. [CrossRef]
15. Gorsevski, V.; Taha, H.; Quattrochi, D.; Luvall, J. Air pollution prevention through urban heat island mitigation: An update on the Urban Heat Island Pilot Project. *Proc. ACEEE Summer Study* **1998**, *9*, 23–32.
16. Kolokotroni, M. Night ventilation cooling of office buildings: Parametric analyses of conceptual energy impacts/Discussion. *Ashrae Trans.* **2001**, *107*, 479.
17. Stone, B.; Hess, J.J.; Frumkin, H. Urban form and extreme heat events: Are sprawling cities more vulnerable to climate change than compact cities? *Environ. Health Perspect.* **2010**, *118*, 1425–1428. [CrossRef] [PubMed]
18. Akbari, H.; Rose, L.S. Urban surfaces and heat island mitigation potentials. *J. Hum. Environ. Stud.* **2008**, *11*, 85–101. [CrossRef]
19. Asaeda, T.; Ca, V.T.; Wake, A. Heat storage of pavement and its effect on the lower atmosphere. *Atmos. Environ.* **1996**, *30*, 413–427. [CrossRef]
20. Takebayashi, H.; Moriyama, M. Study on surface heat budget of various pavements for urban heat island mitigation. *Adv. Mater. Sci. Eng.* **2012**, *2012*, 523051. [CrossRef]
21. Li, H.; Harvey, J.; Kendall, A. Field measurement of albedo for different land cover materials and effects on thermal performance. *Build. Environ.* **2013**, *59*, 536–546. [CrossRef]
22. Morovatdar, A.; Ashtiani, R.S.; Licon, C.; Tirado, C.; Mahmoud, E. Novel framework for the quantification of pavement damages in the overload corridors. *Transp. Res. Rec.* **2020**, *2674*, 179–191. [CrossRef]
23. Wen, C.D.; Mudawar, I. Modeling the effects of surface roughness on the emissivity of aluminum alloys. *Int. J. Heat Mass Transf.* **2006**, *49*, 4279–4289. [CrossRef]
24. Wen, C.D.; Mudawar, I. Emissivity characteristics of polished aluminum alloy surfaces and assessment of multispectral radiation thermometry (MRT) emissivity models. *Int. J. Heat Mass Transf.* **2005**, *48*, 1316–1329. [CrossRef]

25. Wen, C.D.; Mudawar, I. Emissivity characteristics of roughened aluminum alloy surfaces and assessment of multispectral radiation thermometry (MRT) emissivity models. *Int. J. Heat Mass Transf.* **2004**, *47*, 3591–3605. [CrossRef]
26. Wieczorowski, M.; Rozanski, L. Roughness aspects in thermal analysis of machine tools. In Proceedings of the XVIII IMEKO World Congress Metrology for a Sustainable Development, Rio de Janeiro, Brazil, 17–22 September 2006; Volume 2, p. 1701.
27. Qin, Y. Urban canyon albedo and its implication on the use of reflective cool pavements. *Energy Build.* **2015**, *96*, 86–94. [CrossRef]
28. Yaghoobian, N.; Kleissl, J. Effect of reflective pavements on building energy use. *Urban Clim.* **2012**, *2*, 25–42. [CrossRef]
29. Akbari, H.; Pomerantz, M.; Taha, H. Cool surfaces and shade trees to reduce energy use and improve air quality in urban areas. *Sol. Energy* **2001**, *70*, 295–310. [CrossRef]
30. Richard, C.; Dore, G.; Lemieux, C.; Bilodeau, J.P.; Haure-Touze, J. Albedo of pavement surfacing materials: In situ measurements. In Proceedings of the 16th International Conference on Cold Regions Engineering, Salt Lake City, UT, USA, 19–22 July 2015; pp. 181–192.
31. Berdahl, P.; Bretz, S.E. Preliminary survey of the solar reflectance of cool roofing materials. *Energy Build.* **1997**, *25*, 149–158. [CrossRef]
32. Doulos, L.; Santamouris, M.; Livada, I. Passive cooling of outdoor urban spaces. The role of materials. *Sol. Energy* **2004**, *77*, 231–249.
33. Bobes-Jesus, V.; Pascual-Muñoz, P.; Castro-Fresno, D.; Rodriguez-Hernandez, J. Asphalt solar collectors: A literature review. *Appl. Energy* **2013**, *102*, 962–970. [CrossRef]
34. Higashiyama, H.; Sano, M.; Nakanishi, F.; Takahashi, O.; Tsukuma, S. Field measurements of road surface temperature of several asphalt pavements with temperature rise reducing function. *Case Stud. Constr. Mater.* **2016**, *4*, 73–80. [CrossRef]
35. Wan, W.C.; Hien, W.N.; Ping, T.P.; Aloysius, A.Z.W. A study on the effectiveness of heat mitigating pavement coatings in Singapore. *J. Heat Island Inst. Int.* **2012**, *7*, 238–247.
36. Sarat, A.A.; Eusuf, M.A. An experimental study on observed heating characteristics of urban pavement. *J. Surv. Constr. Prop.* **2012**, *3*, 1–12. [CrossRef]
37. Johnsson, J.; Adl-Zarrabi, B. A numerical and experimental study of a pavement solar collector for the northern hemisphere. *Appl. Energy* **2020**, *260*, 114286. [CrossRef]
38. Masoumi, A.P.; Tajalli-Ardekani, E.; Golneshan, A.A. Investigation on performance of an asphalt solar collector: CFD analysis, experimental validation and neural network modeling. *Sol. Energy* **2020**, *207*, 703–719. [CrossRef]
39. Swanson, M.; Hobbs, A. Urban heat island effect: Comparing thermal and radiation effects of asphalt and concrete pavements on adjacent buildings using CFD methods. *Contact Urticaria Syndr.* **2014**, *33*, 1–9.
40. Blocken, B.; Stathopoulos, T.; Saathoff, P.; Wang, X. Numerical evaluation of pollutant dispersion in the built environment: Comparisons between models and experiments. *J. Wind Eng. Ind. Aerodyn.* **2008**, *96*, 1817–1831. [CrossRef]
41. Gousseau, P.; Blocken, B.; Stathopoulos, T.; Van Heijst, G.J.F. CFD simulation of near-field pollutant dispersion on a high-resolution grid: A case study by LES and RANS for a building group in downtown Montreal. *Atmos. Environ.* **2011**, *45*, 428–438. [CrossRef]
42. Tominaga, Y.; Stathopoulos, T. CFD simulation of near-field pollutant dispersion in the urban environment: A review of current modeling techniques. *Atmos. Environ.* **2013**, *79*, 716–730. [CrossRef]
43. Di Sabatino, S.; Buccolieri, R.; Salizzoni, P. Recent advancements in numerical modelling of flow and dispersion in urban areas: A short review. *Int. J. Environ. Pollut.* **2013**, *52*, 172–191. [CrossRef]
44. Kato, S.; Murakami, S.; Mochida, A.; Akabayashi, S.; Tominaga, Y. Velocity-pressure field of cross ventilation with open windows analyzed by wind tunnel and numerical simulation. *J. Wind Eng. Ind. Aerodyn.* **1992**, *44*, 2575–2586. [CrossRef]
45. Ramponi, R.; Blocken, B. CFD simulation of cross-ventilation for a generic isolated building: Impact of computational parameters. *Build. Environ.* **2012**, *53*, 34–48. [CrossRef]
46. Mochida, A.; Lun, I.Y.F. Prediction of wind environment and thermal comfort at pedestrian level in urban area. *J. Wind Eng. Ind. Aerodyn.* **2008**, *96*, 1498–1527. [CrossRef]
47. Murakami, S.; Ooka, R.; Mochida, A.; Yoshida, S. CFD analysis of wind climate from human scale to urban scale. *J. Wind Eng. Ind. Aerodyn.* **1999**, *81*, 57–81. [CrossRef]
48. Stathopoulos, T. Pedestrian level winds and outdoor human comfort. *J. Wind Eng. Ind. Aerodyn.* **2006**, *94*, 769–780. [CrossRef]
49. Yoshie, R.; Mochida, A.; Tominaga, Y.; Kataoka, H.; Harimoto, K.; Nozu, T.; Shirasawa, T. Cooperative project for CFD prediction of pedestrian wind environment in the Architectural Institute of Japan. *J. Wind Eng. Ind. Aerodyn.* **2007**, *95*, 1551–1578. [CrossRef]
50. Nasir, D.S.; Hughes, B.R.; Calautit, J.K. A CFD analysis of several design parameters of a road pavement solar collector (RPSC) for urban application. *Appl. Energy.* **2017**, *186*, 436–449. [CrossRef]
51. Takahashi, K.; Yoshida, H.; Tanaka, Y.; Aotake, N.; Wang, F. Measurement of thermal environment in Kyoto city and its prediction by CFD simulation. *Energy Build.* **2004**, *36*, 771–779. [CrossRef]
52. Nazarian, N.; Kleissl, J. Realistic solar heating in urban areas: Air exchange and street-canyon ventilation. *Build. Environ.* **2016**, *95*, 75–93. [CrossRef]
53. Ng, S.C.; Low, K.S.; Tioh, N.H. Newspaper sandwiched aerated lightweight concrete wall panels—Thermal inertia, transient thermal behavior and surface temperature prediction. *Energy Build.* **2011**, *43*, 1636–1645. [CrossRef]
54. ANSYS Fluent Tutorial Guide Release 18 January 2017. Available online: http://users.abo.fi/rzevenho/ansys%20fluent%2018%20tutorial%20guide.pdf (accessed on 1 June 2020).

55. Woldu, Y.; Fritz, A. Using CFD to Analyze Thermal and Optical Influence on a Zero Pressure Balloon at Floating Condition. Master's Thesis, Lulea University of Technology, Lulea, Sweden, 2018.
56. Moon, J.H.; Lee, J.W.; Jeong, C.H.; Lee, S.H. Thermal comfort analysis in a passenger compartment considering the solar radiation effect. *Int. J. Therm. Sci.* **2016**, *107*, 77–88. [CrossRef]
57. Ajay, K.; Lal, K. Experimental and CFD investigation on the efficiency of parabolic solar collector involving Al_2O_3/H_2O (DI) nanofluid as a working fluid. *Int. J. Renew. Energy Res.* **2016**, *6*, 392–401.
58. Adeniyi, A.A.; Mohammed, A.; Aladeniyi, K. Analysis of a solar dryer box with ray tracing CFD technique. *Int. J. Sci. Res.* **2012**, *3*, 1–5.
59. Jonsson, J. Including Solar Load in CFD Analysis of Temperature Distribution in a Car Passenger Compartment. Master's Thesis, Lulea University of Technology, Lulea, Sweden, 2007.
60. ISO 7730:2005. Ergonomics of the Thermal Environment-Analytical Determination and Interpretation of Thermal Comfort Using Calculation of the PMV and PPD Indices and Local Thermal Comfort Criteria. 2005. Available online: https://www.iso.org/standard/39155.html (accessed on 1 September 2021).
61. Launder, B.E.; Spalding, D.B. The Numerical Computation of Turbulent Flows. *Comput. Methods Appl. Mech. Eng.* **1974**, *3*, 269–289. [CrossRef]
62. Yu, B.; Lu, Q. Estimation of albedo effect in pavement life cycle assessment. *J. Clean. Prod.* **2014**, *64*, 306–309. [CrossRef]
63. Kaloush, K.E.; Carlson, J.D.; Golden, J.S.; Phelan, P.E. *The Thermal and Radiative Characteristics of Concrete Pavements in Mitigating Urban Heat Island Effects*; (No. PCA R&D SN2969); Portland Cement Association: Skokie, IL, USA, 2008.
64. Jeanjean, A.; Olives, R.; Py, X. Selection criteria of thermal mass materials for low-energy building construction applied to conventional and alternative materials. *Energy Build.* **2013**, *63*, 36–48. [CrossRef]
65. Dehdezi, P.K.; Hall, M.R.; Dawson, A. Thermophysical optimization of specialized concrete pavement materials for collection of surface heat energy and applications for shallow heat storage. *Transp. Res. Rec.* **2011**, *2240*, 96–106. [CrossRef]
66. Qin, Y.; Hiller, J.E. Understanding pavement-surface energy balance and its implications on cool pavement development. *Energy Build.* **2014**, *85*, 389–399. [CrossRef]